Journal of
Materials Chemistry A

PAPER

View Article Online
View Journal | View Issue

Cite this: *J. Mater. Chem. A*, 2019, **7**, 24281

The effect of Ag alloying of $Cu_2(Zn,Cd)SnS_4$ on the monograin powder properties and solar cell performance†

Kristi Timmo, *[a] Mare Altosaar,[a] Maris Pilvet,[a] Valdek Mikli,[a] Maarja Grossberg,[a] Mati Danilson,[a] Taavi Raadik,[a] Raavo Josepson,[b] Jüri Krustok[b] and Marit Kauk-Kuusik[a]

Received 17th July 2019
Accepted 6th October 2019

DOI: 10.1039/c9ta07768e

rsc.li/materials-a

Cation substitution in $Cu_2ZnSn(S,Se)_4$ offers a path to improved solar cell device performance through the modification of the structural, optical and electrical properties of the absorber material. In the present study, the effect of partial substitution of copper with silver in $Cu_{1.85}(Zn_{0.8}Cd_{0.2})_{1.1}SnS_4$ monograin powders was investigated. $(Cu_{1-x}Ag_x)_{1.85}(Zn_{0.8}Cd_{0.2})_{1.1}SnS_4$ (ACZCTS) monograin powders with different ratios of [Ag]/([Cu] + [Ag]) were synthesized from CuS, Ag_2S, ZnS, CdS, SnS and elemental sulfur in the liquid phase of KI as the flux material in evacuated quartz ampoules at 740 °C. EDX analysis of the as-grown materials in the entire series revealed that the Ag concentration was different in the synthesized materials than in the corresponding precursor mixtures. Furthermore, the Ag concentration at the surface of crystals was found to be higher than in the bulk of crystals. By increasing the input Ag content, the shape of grown crystals changed from sharp edged tetragonal to a more rounded form. Raman spectra showed a shift in the A peak position from 336 to 334 cm^{-1} as the Ag content increased in $(Cu_{1-x}Ag_x)_{1.85}(Zn_{0.8}Cd_{0.2})_{1.1}SnS_4$. The changes in the recombination processes were studied by temperature dependent photoluminescence spectroscopy and current–voltage characteristics analysis. It was found that the acceptor concentration in the absorber can be modified by varying the Ag content in ACZCTS. The incorporation of Ag into the $Cu_{1.85}(Zn_{0.8}Cd_{0.2})_{1.1}SnS_4$ monograin absorber material improved the efficiency of monograin layer solar cells from 6.62% ($x = 0$) to 8.73% ($x = 0.01$).

1. Introduction

Kesterite materials are currently the most promising emerging absorber materials for fully inorganic thin film photovoltaic technology based on critical raw-material-free and sustainable solutions.[1] The record conversion efficiency of kesterites of 12.6% was achieved in 2014 (ref. 2) and it has not been surpassed yet. The large open circuit voltage (V_{oc}) deficit of kesterite solar cells is still a matter of intensive research. Most of the studies on kesterite materials have shown a very high concentration of point defects and extremely low formation energies of different defect clusters in $Cu_2ZnSn(S,Se)_4$ (CZTSSe) which are detrimental to solar cell parameters. One method to reduce the number of antisite defects is the replacement of Cu (or Zn) with isoelectronic elements that have larger covalent radii, such as Ag (or Cd), to increase the energy barrier for site exchange with Zn. Substitution of Cu with Ag more than doubles the formation energy for anti-site defects, which should result in an order of magnitude lower density of defects.[3,4] Chagarov *et al.* concluded from density functional theory calculations that the optoelectronic properties of $Ag_2ZnSnSe_4$ are more similar to those of $Cu(In,Ga)Se_2$ than to those of CZTSSe giving the opportunity for overcoming the performance limitations observed in the kesterite systems.[3] It was shown in previous experimental studies that the maximum device performances were obtained for partial cation substitution with the optimum concentration ratio of $Ag/(Ag + Cu) = 0.03–0.10$ in the case of Ag,[5–8] $Cd/(Cd + Zn) = 0.05–0.4$ in the case of Cd[9–11] and $Ge/(Ge + Sn) = 0.22–0.4$ (ref. 12–14) in the case of Ge. It was found by S. H. Hadke *et al.* that double cation substitution (partial replacement of Cu with Ag and Zn with Cd) could be one possible way to improve the device performance.[15] They achieved a 10.1% total-area power conversion efficiency of CZTS solar cells at a composition of 5% Ag + 25% Cd with respect to Cu and Zn, respectively. Furthermore, the increased concentrations of Ag and Cd at crystals' surfaces could have a positive effect on the solar cell performance due to the formed graded surface layer, as it was found by J. F. Qi *et al.*, who intentionally formed Ag-rich graded absorber surface layers.[6] They reported

---

[a] *Department of Materials and Environmental Technology, Tallinn University of Technology, Ehitajate tee 5, 19086 Tallinn, Estonia. E-mail: kristi.timmo@taltech.ee*

[b] *Division of Physics, Tallinn University of Technology, Ehitajate tee 5, 19086 Tallinn, Estonia*

† Electronic supplementary information (ESI) available. See DOI: 10.1039/c9ta07768e

the positive effect of the Ag-graded structure with a higher Ag content on both, the back and front surfaces of the $(Cu,Ag)_2ZnSn(S,Se)_4$ thin film layer. As a result, they demonstrated a conversion efficiency of 11.2% through a significant increase in the V_{oc} values due to the improved Fermi level pinning at the CdS/absorber interface and depressed recombination at the absorber/Mo interface. However, the effects of Ag and Cd substitution on the properties of the CZTS absorber material are diverse. G. S. Gautam *et al.*[16] found by theoretical calculations that Cd in CZTS at a low level could suppress disorder in the kesterite phase across all Cu concentrations, whereas a higher Cd content could stabilize the lower-gap stannite structure; a low level Ag doping could suppress disorder when Zn- and Sn-rich conditions are employed.

In this study the molten salt synthesis–growth method is used for the synthesis of $(Cu_{1-x}Ag_x)_{1.85}(Zn_{0.8}Cd_{0.2})_{1.1}SnS_4$ (ACZCTS) monograin powders with different x values ($0 < x \leq 0.15$) in KI (as flux). In the molten salt method large amounts of a salt are used to avoid sintering of crystals. At the same time, in thin film technology, molten phase sintering of polycrystals with concurrent recrystallization and crystal growth in the presence of a limited amount of some formed liquid phase (for example Na_2Se_x)[17] is extremely recommended. However, the role of the formed liquid phase as a possible solvent for constituent elements in thin films as well as in the molten salt synthesis is not thoroughly studied. KI as a solvent was found to be chemically inactive in the synthesis of CZTSe[18] and $CuInSe_2$ (ref. 19) monograin powders; however, different solubilities of the used precursor compounds (CuSe, ZnSe, and SnSe) in KI were determined. It should be mentioned that KI is also an inexhaustible source for potassium and iodine doping. The solubility of potassium and iodine at 720 °C was found to be 0.094 wt% and 0.0086 wt% in $CuInSe_2$ (ref. 19) and 0.01–0.02 wt% in CZTSe,[18] respectively. The interaction of Ag_2S with molten KI was not studied by us before; therefore, as a novelty the distribution of Ag (Ag_2S) between liquid KI and solid $(Cu_{1-x}Ag_x)_{1.85}(Zn_{0.8}Cd_{0.2})_{1.1}SnS_4$ phases is studied in the present work.

By using monograin powder crystal growth in molten potassium iodide, we demonstrate that Ag substitution of Cu in ACZCTS can be achieved in the range of used concentrations depending on the distribution of Ag between solid and liquid phases. As a result, a Ag-rich crystal surface was formed after synthesis. The concentration ratio $[Ag]_{surface}/[Ag]_{bulk} = 2$ was determined for all the used x values. The modified flux composition had an impact on the morphology of the formed ACZCTS crystals. Due to the distribution of Ag the standard monograin powder preparation technology had to be modified. The effect of partial substitution of Cu with Ag on the $Cu_{1.85}(Zn_{0.8}Cd_{0.2})_{1.1}SnS_4$ monograin powder properties is investigated. Our findings confirm that the positive effect of Ag incorporation on the monograin layer (MGL) solar cell working ability appears only at very low Ag concentrations while higher levels are detrimental to the solar cell performance. As a result of the optimization of initial composition ([Ag]/([Cu] + [Ag]) ratio) for the growth of ACZCTS monograin powder crystals the MGL solar cell efficiency improved from 6.62% to 8.73%. For the Ag and Cd containing kesterite solar cells, the analysis of the behavior of the ideality factor depending on the Ag content and temperature is presented for the first time.

2. Experimental

2.1 Preparation of ACZCTS monograin powders

$(Cu_{1-x}Ag_x)_{1.85}(Zn_{0.8}Cd_{0.2})_{1.1}SnS_4$ (ACZCTS) monograin powders with different x values ($x = 0$, 0.01, 0.02, 0.03, 0.04, 0.05, 0.1 and 0.15) were prepared from binary compounds in the liquid phase of KI as the flux material. Hereafter all x values are presented as atomic percentages of Ag for Cu substitution ($x = 0$, 1, 2, 3, 4, 5, 10, and 15%). The used precursor compounds CuS (3N), Ag_2S (4N) and SnS (3N) were self-synthesized in evacuated quartz ampoules, and ZnS (5N) and CdS (5N) were commercially available. As the flux material, water-soluble potassium iodide was used with the volume ratio of KI to ACZCTS equal to 1 ($cm^3\ cm^{-3}$). KI was dehydrated in the dynamic vacuum-pumping process by heating at temperatures up to 270 °C. The precursors were weighed in desired amounts and ratios, mixed in a ball mill, loaded into quartz ampoules, degassed under dynamic vacuum, sealed and heated isothermally at 740 °C for 142 hours. The growth processes were stopped by cooling the ampoules to room temperature. The flux material was removed by leaching and rinsing with deionized water. The released monograin powders were dried in a hot-air thermostat and sieved into several narrow granulometric fractions between 38 and 112 μm.

The as-grown ACZCTS monograin powders with varied Ag content were etched by using combined chemical etching worked out for kesterite monograin powders[20] (1% Br_2 in methanol solution for 10 minutes followed by etching with 10% aqueous KCN solution for 10 minutes) with the aim of removing from the crystals' surfaces the solids that precipitated from molten KI. Some part of precursors and formed ACZCTS compound dissolve in molten KI at the synthesis–growth temperature (740 °C) and this dissolved part deposits onto crystals' surfaces in the cooling process as solids due to the decrease in solubility at lower temperatures.[20] After the etching process, the materials were annealed in sealed ampoules in a two-temperature-zone furnace at 840 °C in a sulfur atmosphere of 2050 Torr for 1 hour to heal the surface imperfections generated by etching and to adjust the surface composition.

2.2 Preparation of ACZCTS monograin layer solar cells

The post-treated monograin powders were used as absorber materials in monograin layer (MGL) solar cells with the structure of graphite/ACZCTS/CdS/i-ZnO/ZnO:Al/Ag/glass. In MGL solar cells every ACZCTS crystal works as an individual tiny solar cell in parallel connection. The scheme and cross-sectional view of the MGL solar cells structure can be found in the ESI (Fig. S1 and S2, ESI†). The post-treated powder crystals were covered with CdS by the chemical bath deposition (CBD) method and sieved into narrow size-fractions for making photoactive MGLs (membranes). In a membrane the ACZCTS crystals stand separately without contacting each other and are bound together with a thin layer of epoxy. The used size range of powder crystals determines the thickness of the absorber layer (for example 45–56 µm, 56–63 µm, 63–75 µm, 75–80 µm, 80–90 µm, 90–100 µm, *etc.*). Before CdS buffer layer deposition, short time (a few seconds) combined etching (Br_2 in methanol + KCN) at RT was used, as reported in our previous work.[21] The photoactive MGL (membrane) was formed by embedding the CdS covered ACZCTS crystals halfway to a thin epoxy layer (on a supporting plastic foil substrate). The thickness of the epoxy layer is determined by the size of the grains used for membrane preparation. After polymerization of the epoxy, the membranes were covered with an i-ZnO layer with a thickness of about 40–45 nm and a conductive ZnO:Al layer with a thickness of about 350–400 nm using a radio frequency magnetron sputtering system to act as a top electrode.

Finally, to intensify the collection of charge carriers, conductive silver paste grid contacts were applied on top of the bilayer of the ZnO window, and the structure was glued onto a glass substrate. After removal of the supporting plastic foil from the structure, the surfaces of powder crystals at the back contact side were released partly from the epoxy by etching with concentrated H_2SO_4 for determined times. Finally, a mechanical abrasive treatment was applied to open the back contact area of crystals. Subsequently, the back contact was made with graphite conductive paste.

2.3 Characterization

The chemical composition of untreated powder crystals was determined by energy dispersive X-ray spectroscopy (EDX) using a Bruker Esprit 1.8 system (the measurement error is about 0.5 at%). The shape and surface morphology of the synthesized crystals were studied with a high-resolution scanning electron microscope (SEM), Zeiss MERLIN. The micro-Raman spectra were recorded by using a Horiba LabRam HR800 spectrometer and a 532 nm laser line that was focused on the sample with a spot size of about 5 µm. Powder X-ray diffraction (XRD) patterns were recorded on a Rigaku Ultima IV diffractometer with Cu K_α radiation ($\lambda = 1.5406$ Å). PDXL 2 software was used for the derivation of crystal structure information from powder XRD data. For photoluminescence (PL) measurements, the powder samples were mounted in a closed-cycle He cryostat and cooled down to 10 K. A 441 nm He–Cd laser line was used for PL excitation and the spectra were detected by using an InGaAs detector. For the low-temperature PL measurements a focused laser beam with a spot size of about 3 mm was used. It means that the PL spectrum corresponds to at least 400 crystals. The measurement error in the values of the PL peak positions is 0.005 eV.

The solar cells were characterized by measuring the current *versus* voltage (*J*–*V*) characteristics with a Keithley 2400 electrometer under standard test conditions (AM 1.5, 100 mW cm^{-2}) obtained using a Newport solar simulator. The measurement error in V_{oc} values can be considered to be up to 10 mV. As the working area of the MGL solar cells is around 75% of the total area,[22] the MGL solar cell efficiency values were recalculated for the active area (η_{active}). The top view of the packing density of crystals in the membrane can be found in the ESI (Fig. S3, ESI†). Spectral response measurements were performed using a computer controlled SPM-2 prism monochromator. The generated photocurrent was detected at 0 V bias voltage at RT by using a 250 W halogen lamp. Temperature-dependent *J*–*V* curve measurements were made by using an Autolab PGSTAT system. The solar cells were mounted on the cold finger of a closed-cycle He cryostat ($T = 20$–320 K).

3. Results and discussion

The shape and surface morphology of the synthesized $(Cu_{1-x}Ag_x)_{1.85}(Zn_{0.8}Cd_{0.2})_{1.1}SnS_4$ monograin powder crystals were characterized by SEM and the composition by EDX. In Fig. 1, the SEM images of the most distinctive powder crystals – without Ag ($x = 0\%$) (Fig. 1a–c) and with the highest added Ag content ($x = 15\%$) for Cu substitution – are presented (Fig. 1d–f). The monograin powder crystals without Ag (see Fig. 1a–c) and with low Ag contents ($x = 1$–5%, not shown) have a tetragonal shape with rather sharp edges and smooth flat planes typical of the CZTS crystals formed in the monograin synthesis–growth in KI where the solubility of the target compound is low (for example the solubility of $Cu_2ZnSnSe_4$ in KI was determined as 0.61 mol% at $T = 740$ °C).[23] The increase in the Ag content ($x \geq 10\%$) in the precursor mixtures for ACZCTS caused the formation of monograins with more rounded edges and more rough crystal surfaces (see Fig. 1d–f). The synthesis–growth process is performed in closed ampoules under isothermal conditions. Therefore, the only driving force for the crystal growth is the difference in the surface energies of crystals with different sizes and at different places (areas) of individual crystals (surface energy at grain edges is higher than at plain surfaces).[24] Thus, different processes are concurrently taking place – the dissolution of smaller crystals and growth of bigger crystals, and the diffusion of material through the molten phase and on the facets of crystals. If the dissolution is faster (from edges due to higher surface energy) than the growth (on planes) then more rounded crystals form. The dissolution is faster if the solubility is higher. The growth is faster when the liquid phase is richer with constituent elements. Therefore, the possible explanation for the growth of more rounded crystals with an increased Ag-content is that the solubility of ACZCTS (or its precursors) in KI is higher than that of pure CZCTS.[25] The reason for the formation of more rough crystal surfaces with increasing Ag content could be the formation of a modified molten phase composition due to the solvation. It is known that new compounds or solid solutions of them can form in the molten flux used in the synthesis–growth process.[26,27] On the basis of literature data, the probable compounds formed in KI in the solvation process could be Ag–Cd–S (most probable), K–Ag–I or AgI.[28,29] As K–Ag–I compounds are in the molten phase at the used growth temperature of 740 °C, and if formed, they could act as liquid components in the molten phase and modify the composition of flux. It is shown in our previous studies[20,30] that this part of compounds (precursors and formed products) dissolved in KI at growth temperature precipitates out during the cooling process. Part of the dissolved material diffuses onto

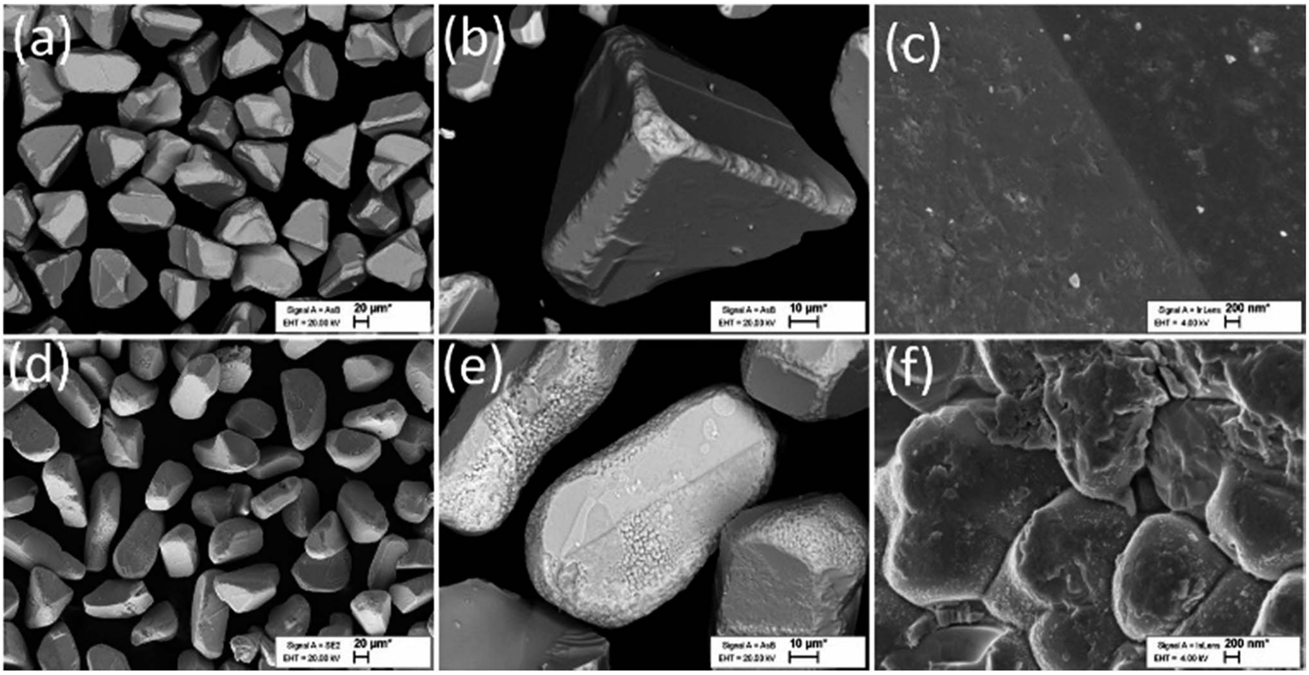

Fig. 1 SEM images of $(Cu_{1-x}Ag_x)_{1.85}(Zn_{0.8}Cd_{0.2})_{1.1}SnS_4$ monograin powder crystals and crystals' surfaces with $x = 0\%$ (a–c) and $x = 15\%$ (d–f).

solid grown crystals forming a crust on crystal surfaces and the other part remains in the solidified KI as amorphous residues.

The EDX elemental mapping of Ag, Cd, Cu, Zn, Sn and S for polished as-grown ACZCTS crystals with 15% input Ag (ratio of $[Ag]/([Cu] + [Ag]) = 0.15$) is presented in Fig. 2a. The EDX elemental mapping for polished as-grown ACZCTS crystals without and with 1% input Ag is shown in the ESI (Fig. S4, ESI†). Fig. 2b shows the EDX line scan over the cross-section of an ACZCTS polished crystal of the same powder. EDX analysis (scan and mapping) indicates the Ag- and Cd-rich surface on the grains, while the Cu content on the surface is decreased compared to its constant value in the bulk of the monograins. The concentrations of Sn, Zn and S are constant over the polished crystals. However, we can recognize a place where ZnS is enclosed into a surrounding ACZCTS crystal. Such a phenomenon can occur if the ZnS compound (with high melting temperature and low vapour pressure) is used as the precursor for Zn. Considering EDX data, it is most probable that the Ag- and Cd-rich surface crust of crystals is formed as a result of precipitation of Ag–Cd–S from KI-flux during the cooling process. The fact that the concentration of Ag in the bulk of grown crystals (black squares in Fig. 3) is almost two times lower than the Ag concentration in the surface crust (blue stars) (being nearly equal to the Ag content in the input precursor mixtures) is proof that there is distribution of Ag between liquid (flux) and solid (ACZCTS) phases. From the gained results we can conclude that the Ag distribution between liquid and solid phases in the studied system can be characterized using the ratio of $[Ag]_{surface}/[Ag]_{bulk}$. The concentration ratio $[Ag]_{surface}/[Ag]_{bulk} = 2$ was determined for all the used x values. The concentration of Ag was also determined in the post-annealed crystals. The EDX analyses revealed that the concentration of Ag in the bulk was increased after the post heat-treatment and the concentration ratios of Ag/(Cu + Ag) (at%) in the surface and in the bulk were equalized (compare black solid squares with black empty squares in Fig. 3). The increase in Ag concentration in the bulk after post heat-treatment can be possible at the expense of its higher surface concentrations if Ag from the surface crust diffuses and distributes homogeneously in the bulk of the crystals. The comparison of EDX line scans from untreated (as-grown) and post-treated crystals can be seen in Fig. 2b and c. From such behavior we can conclude that the distribution of Ag (Ag_2S) between liquid and solid phases in the molten salt synthesis–growth process is limiting the incorporation of Ag into the ACZCTS crystals grown in KI.

X-ray diffraction patterns of monograin powders of $(Cu_{1-x}Ag_x)_{1.85}(Zn_{0.8}Cd_{0.2})_{1.1}SnS_4$ with increasing input Ag content $x =$ 0–15% are displayed in Fig. 4a. All the diffraction peaks could be indexed according to a tetragonal kesterite-type phase (ICDD PDF-2 Release 2019 RDB, 01-085-7033) with different Ag contents. No secondary phases were observed from XRD in the as-grown ACZCTS powders. Lattice expansion due to the increasing Cu substitution by Ag ions is seen as a systematic shift of all diffraction peaks toward lower angles. Fig. 4b shows the enlarged view of the (112) lattice plane diffraction peak shift from 28.28 to 28.12 Å, which is in good correlation with the results reported previously.[15,31–34] Using the X-ray diffraction patterns, the values of lattice parameters (a and c) for all the powders were calculated by Rietveld refinement (see Fig. 4c). A linear increase of the lattice parameter values (a from 5.4604 Å to 5.4961 Å and c from 10.9117 Å to 10.9505 Å) was observed upon replacement of copper with silver, since the ionic radius of Ag^+ (1.14 Å) is larger than that of Cu^+ (0.74 Å).[35] The obtained values are in good agreement with the results reported in the

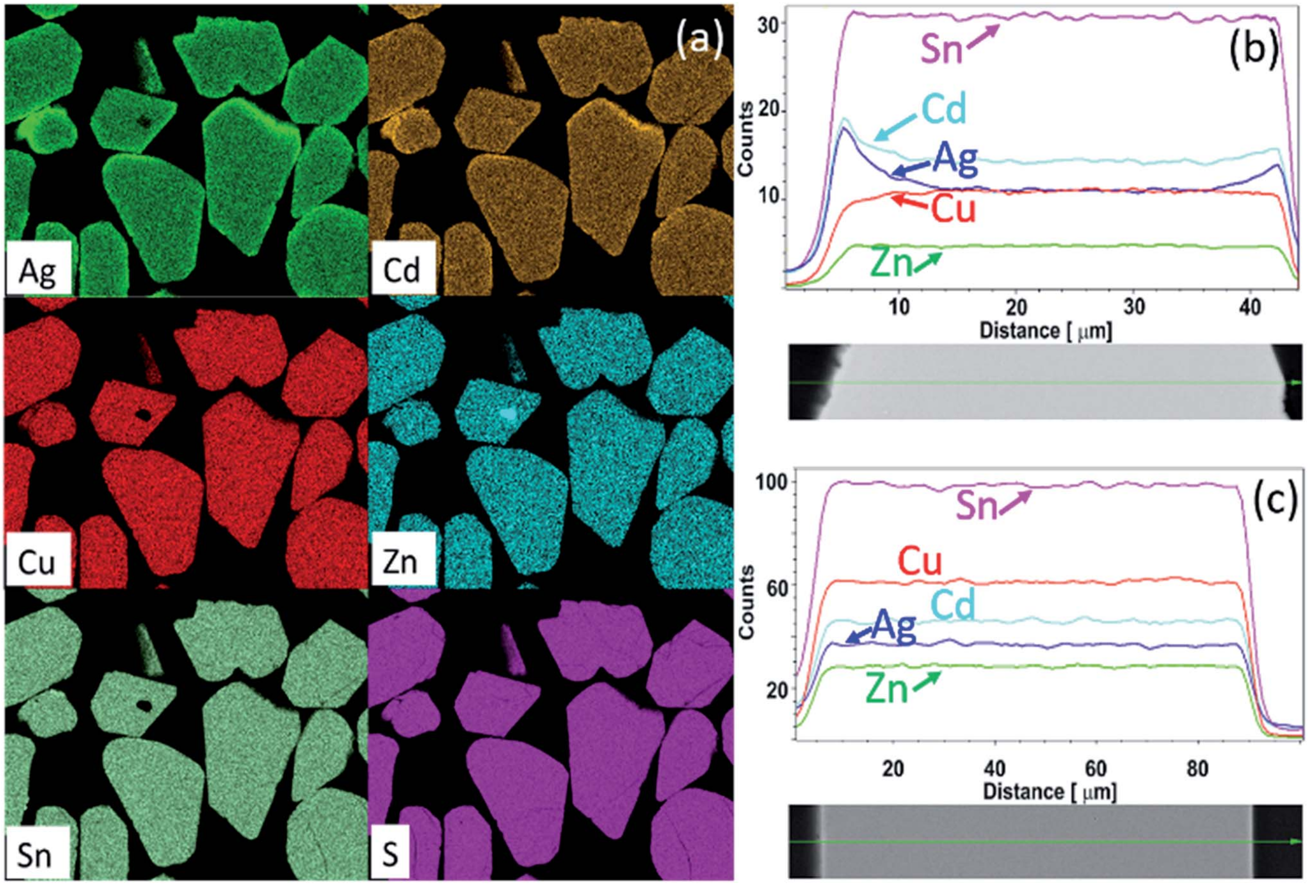

Fig. 2 (a) EDX elemental mapping of Ag, Cd, Cu, Zn, Sn and S for as-grown ACZCTS polished crystals with 15% input Ag (ratio of [Ag]/([Cu] + [Ag]) = 0.15). (b) EDX line scan over the cross-section of a crystal of the same powder and (c) EDX line scan over the cross-section of a post-treated powder crystal.

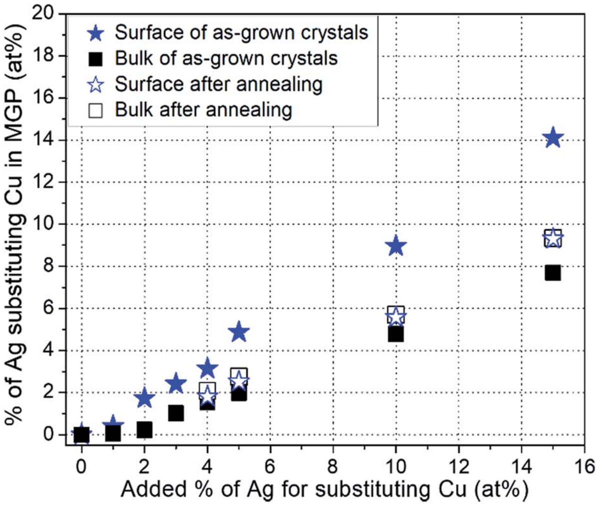

Fig. 3 Concentration ratios of Ag/(Cu + Ag) (at%) in the surface area (blue stars) and in the bulk (black squares) of ACZCTS monograin powder (MGP) crystals (determined by EDX) depending on added Ag content with respect to Cu. Concentration ratios after annealing at 840 °C for 1 h in a sulfur atmosphere of 2050 Torr in the crystals' surface are marked as blue empty stars and in the bulk as black empty squares.

literature for Ag substituted kesterites and suggest that Ag is incorporated in the CZCTS lattice.[31] Balboul *et al.* showed correlation between the $c/2a$ ratio, composition and efficiency in $\mathrm{CuIn}_{1-x}\mathrm{Ga}_x\mathrm{Se}_2$ materials, and concluded that the lowest electronic defect density occurs at $x \approx 0.2$, due to the smallest possible crystallographic distortion of the tetragonal lattice at this composition.[36] Our experiments with ACZCTS monograin powders showed the smallest tetragonal lattice distortion with the $c/2a$ ratio $= 0.9995$ for the input Ag content $x = 1\%$ (Fig. 4c). For the other studied compounds with $x = 0$–15%, the tetragonal distortion is enhanced with the ratio of $c/2a$ changing from 0.9991 to 0.9962.

Raman spectroscopy analysis was carried out to investigate the coexisting secondary phases that cannot be distinguished by XRD in ACZCTS due to the similar XRD patterns of Zn(Cd)S, $\mathrm{Cu_2SnS_3}$ and $\mathrm{Cu_2ZnSnS_4}$.[37–39] Fig. 5a shows the Raman spectra of the post-treated (chemically etched and annealed) ACZCTS monograin powder crystals' surface with different input Ag contents (ratios of [Ag]/([Cu] + [Ag])) from 0 to 15%. The inset graph in Fig. 5a presents the comparison of the untreated and post-treated crystals' surfaces with an input Ag content of 15%. The Raman spectrum of the CZCTS monograin powder crystals exhibited an intense peak centered at 336 cm^{-1} and three weak

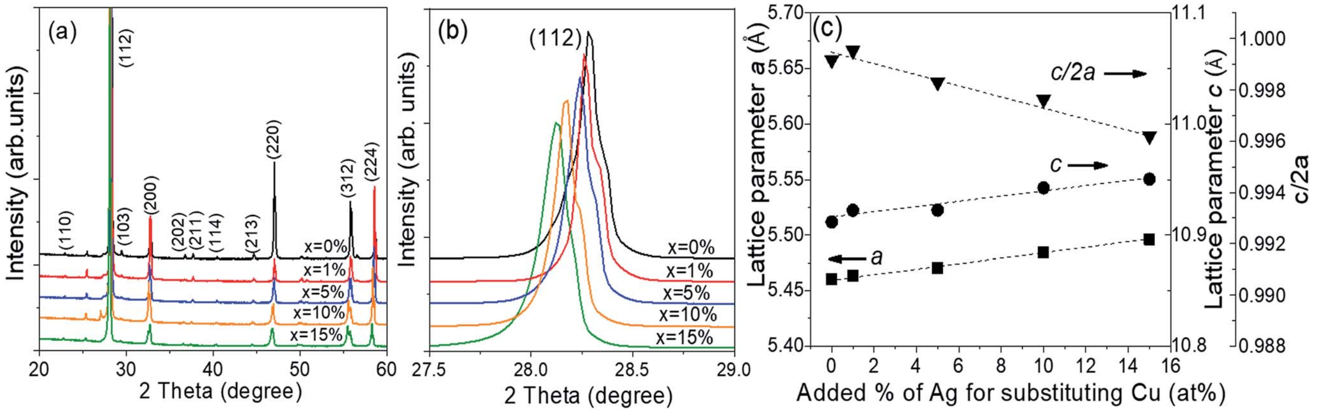

Fig. 4 (a) X-ray diffraction patterns of the $(Cu_{1-x}Ag_x)_{1.85}(Zn_{0.8}Cd_{0.2})_{1.1}SnS_4$ monograin powders with increasing Ag content in the input composition, (b) the shift of the (112) diffraction peak positions and (c) lattice parameters *a*, *c* and *c*/2*a* as a function of the input Ag content. The dashed lines represent the predicted lattice constants from Vegard's law, and the markers represent measured values.

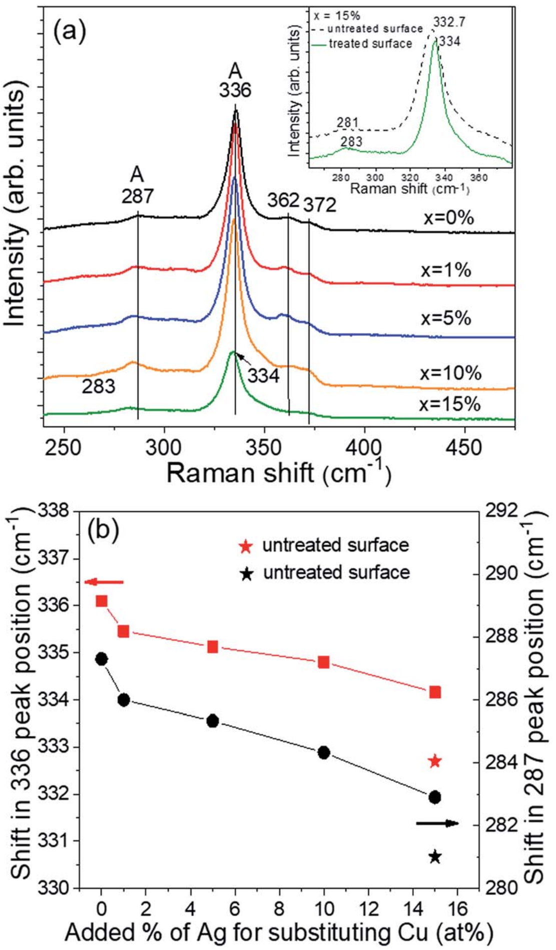

Fig. 5 (a) Raman spectra of the chemically etched and annealed (treated) ACZCTS monograin powder crystals' surface with different added percentages of Ag for Cu substitution ($x = 0$–15%) and the inset graph of (a) shows untreated crystals' surface with an input Ag content of 15%. (b) Peak positions of A modes at 336 and 287 cm^{-1} as a function of the input Ag content in precursors.

peaks at 287, 362 and 372 cm^{-1}. All Raman peaks correspond to the kesterite CZCTS phase and are in good correlation with the results observed in other papers,[10,40] where replacement of Zn with Cd in CZTS was investigated. No secondary phases were detected in the Raman spectra of the crystals.

The change in the frequency of the two A modes (336 and 287 cm^{-1}) of ACZCTS as a function of the input Ag content is presented in Fig. 5b. By increasing the substitution of Cu with Ag, a linear shift towards lower wavenumbers from 336 to 334 cm^{-1} and from 287 to 283 cm^{-1} in the Raman A mode peak frequency was obtained as can be seen in Fig. 5a and b. An even larger shift is seen in the Raman spectra of untreated crystals' surface with a Ag content of 15% (analyzed by EDX). Similar results have been reported for $(Cu,Ag)_2ZnSnS_4$ by T. H. Nguyen *et al.* and for the $(Cu,Ag)_2ZnSn(S,Se)_4$ compound by Zhao *et al.* and Y. Qi *et al.*, who also detected shifts in the main A Raman peak and low wavenumber A peak positions by increasing [Ag]/([Cu] + [Ag]) ratios in thin films.[5,32,33] The shifts of Raman scattering peaks at 336 cm^{-1} and at 287 cm^{-1} to the lower wavenumber side when increasing the Ag content in ACZCTS could be attributed also to the increase in the crystal lattice parameters caused by the substitution of Cu^+ with the heavier and bigger Ag^+. This confirms the results of XRD analysis where it was found that Ag was incorporated into the CZCTS monograin powder crystals' lattice.

Photoluminescence measurements were performed to study the changes in the recombination processes. The photoluminescence (PL) spectra (Fig. 6a) were found to be slightly shifted to the higher energy values with increasing Ag content, which is consistent with the changes in the band gap energy of the material. Temperature and excitation power dependent PL measurements indicate that there is no change in the radiative recombination mechanism (quasi donor–acceptor-pair transition at low temperatures and a free-to-bound transition at high temperatures) for the studied Ag contents as was also found by S. H. Hadke *et al.*[15] The laser power and temperature dependencies of the PL spectra for three $(Cu_{1-x}Ag_x)_{1.85}(Zn_{0.8}Cd_{0.2})_{1.1}SnS_4$ monograin powders with $x = 0$, 1 and 15% are

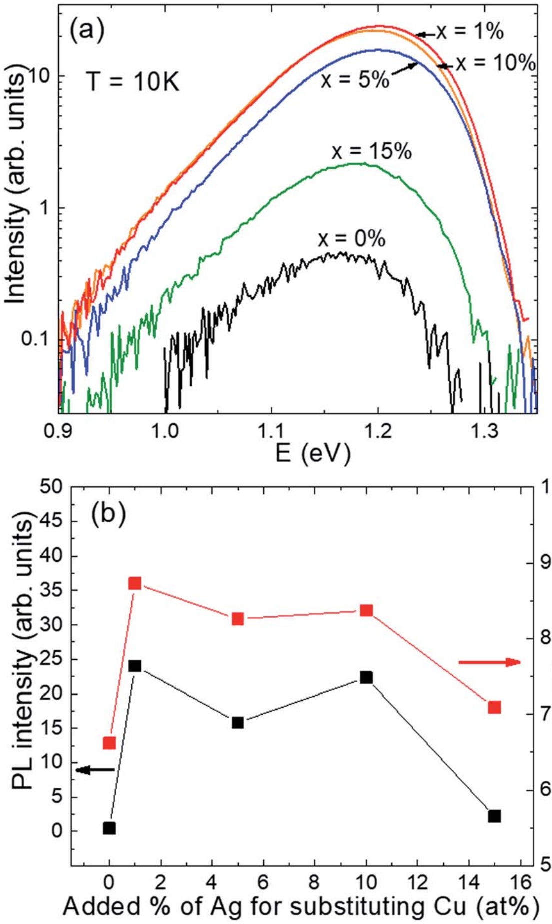

Fig. 6 (a) Low-temperature (T = 10 K) PL spectra of the ACZCTS monograin powders with an input Ag content of 0 to 15%. (b) The dependence of PL intensities of monograin powders and power conversion efficiencies of solar cells on the input Ag content.

shown in Fig. S5 in the ESI.† For all samples, a blue shift of the PL bands with a magnitude of 14 meV per decade was detected as was also detected by S. H. Hadke *et al.* From Fig. S5 (ESI†) one can also see that the PL bands first shift towards lower energies with increasing temperature and starting from about 150 K, towards higher energies resulting from the change in the recombination mechanism to free-to-bound recombination. This was also observed by Hadke *et al.*[15] In addition, the thermal activation energies describing the quenching of the PL emission with temperature were determined, which were slightly different for the three samples (see inset graphs in Fig. S5, ESI†). Interestingly, a strong increase in the PL intensity of the Ag containing materials in comparison to the reference (see Fig. 6a black spectra) is observed. The strongest PL signal was obtained from the powder sample with 1% input Ag with respect to Cu, leading also to the highest efficiency in the case of the corresponding solar cells (Fig. 6b).

All the $(Cu_{1-x}Ag_x)_{1.85}(Zn_{0.8}Cd_{0.2})_{1.1}SnS_4$ monograin powders were used as absorber materials in MGL solar cells after post-treatments (chemical etching and annealing in a sulfur atmosphere). External quantum efficiency (EQE) analysis was used to estimate the effective bandgap energy (E_g^*) values of the synthesized absorber materials since the evaluation of E_g from the optical absorption or reflectance spectra of monograin powders is rather challenging. The EQE of the $(Cu_{1-x}Ag_x)_{1.85}(Zn_{0.8}Cd_{0.2})_{1.1}SnS_4$ MGL solar cells was measured as a function of the incident light wavelength at room temperature (Fig. 7). From the linear segment of the low-energy side of the construction $(EQE)^2$ *vs.* E curves, the E_g^* can be evaluated.[41] The effective band gap energy E_g^* values depending on the Ag content in the absorber material are shown in the inset graph of Fig. 7. A slight increase of the E_g^* from 1.503 eV to 1.528 eV when increasing the Ag content in ACZCTS monograin powder materials was observed.

To further evaluate the influence of the Ag substitution level on MGL solar cell performance, photovoltaic investigations on ACZCTS were carried out. The ACZCTS MGL solar cells' parameters for different Ag concentrations are displayed as box plots in Fig. 8. Data are extrapolated from the analysis of 15 solar cells. A clear correlation between the Ag content in the absorber material and the device performance is found. Table 1 presents the solar cell output parameters of the best performing ACZCTS MGL solar cells for the devices based on the $(Cu_{1-x}Ag_x)_{1.85}(Zn_{0.8}Cd_{0.2})_{1.1}SnS_4$ monograin powders with x = 0, 1, 3, 4, 5, 10 and 15%. Light J–V curves of the $(Cu_{1-x}Ag_x)_{1.85}(Zn_{0.8}Cd_{0.2})_{1.1}SnS_4$ solar cells with different added percentages of Ag for Cu substitution (x = 0, 1, 5, 10, 15%) are shown in the ESI (Fig. S6, ESI†). With the increase of Ag content in the absorber from 0 to 15%, the power conversion efficiency (PCE) of ACZCTS increased from 6.62% (x = 0%) to 8.73% (x = 1%), then decreased slightly and remained at the 8% level for a Ag content of x = 10% (see Table 1). For a higher content of Ag in ACZCTS, the PCE dropped back to 7.09% (x = 15%) due to the decrease in V_{oc} despite the continuous increase in the bandgap energy values. Therefore, according to our results the changes in V_{oc} values due to the addition of Ag in CZCTS cannot be explained with the variations in the band gap of the

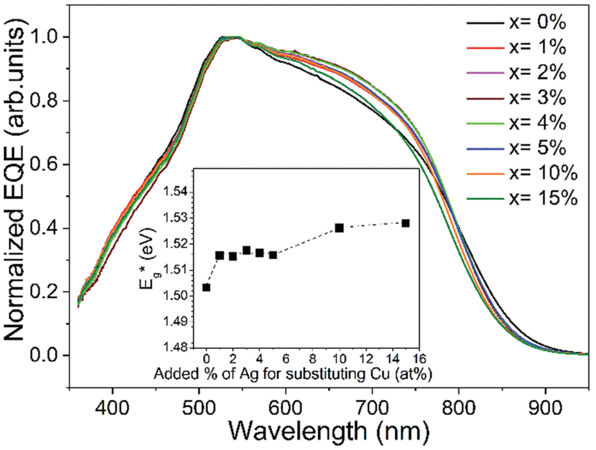

Fig. 7 Normalized external quantum efficiency spectra of $(Cu_{1-x}Ag_x)_{1.85}(Zn_{0.8}Cd_{0.2})_{1.1}SnS_4$ MGL solar cells with increasing Ag content in the input composition. The inset graph presents the effective band gap energy (E_g^*) values depending on the input Ag content.

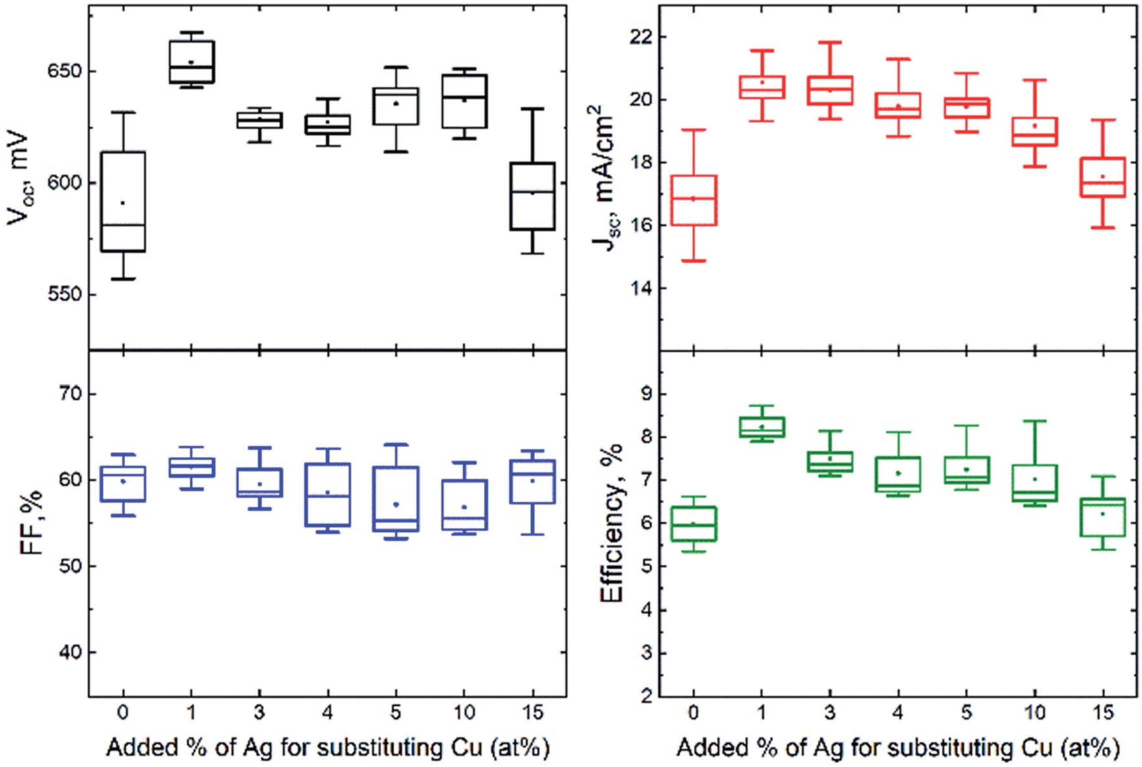

Fig. 8 Box plots of the open circuit voltage, short-circuit current density, fill factor and efficiency of MGL solar cells fabricated from ACZCTS monograin powders with different added Ag contents with respect to Cu.

Table 1 Summary of device parameters for the best performing ACZCTS MGL solar cells depending on Cu replacement with Ag in absorber materials

Added Ag with respect to Cu (%)	V_{oc} (mV)	FF (%)	J_{sc} (mA cm^{-2})	Eff. (%) (active area)	E_g^* (eV)	$E_g/q - V_{oc}$ (mV)	E_{00} (meV)
0	632	62.96	16.65	6.62	1.503	871	37 ± 1
1	664	63.86	20.57	8.73	1.515	851	45 ± 1
3	649	63.77	19.40	8.04	1.517	868	—
4	646	63.50	19.79	8.12	1.516	870	—
5	652	64.11	19.76	8.26	1.516	864	49 ± 1
10	650	61.92	20.81	8.37	1.526	876	61 ± 1
15	633	63.41	17.64	7.09	1.528	895	43 ± 1

absorber and they must be related to the changes in the recombination processes. Since PL analysis showed no change in the radiative recombination mechanism for the studied Ag contents, changes in the non-radiative recombination and/or interface recombination are expected. Notably, all Ag containing cells showed higher PCE values than the CZCTS devices. The open circuit voltage (V_{oc}) and short circuit current density (J_{sc}) values of ACZCTS MGL solar cells followed the same trend as PCE, and at the same time the fill factor (FF) values remained almost constant. Compared to the pure CZCTS device, the V_{oc} and J_{sc} values of the ACZCTS device with an added Ag content of $x = 1\%$ increased from 632 to 664 mV and from 16.65 to 20.57 mA cm^{-2}, respectively. The increase in V_{oc} values of Ag containing solar cells ($x \leq 10\%$) is explained in many papers as an effect of the decrease of Cu_{Zn} antisite defects in absorber materials,[4,6] but other explanations for this increase are also possible.

The most probable reason for the improvement of J_{sc} upon Cu substitution with Ag is related to the decrease of recombination losses. According to Fig. 6b, the PL intensity also increases with Ag incorporation and this increase is similarly caused by the reduction of non-radiative recombination.

Temperature-dependent *J–V* curve measurements were used to further study the recombination mechanisms and to estimate the junction quality. It is known that the temperature dependence near room temperature can be presented as:[42]

$$V_{oc} = \frac{E_A}{q} - \frac{nkT}{q}\ln\left[\frac{J_{00}}{J_L}\right] \qquad (1)$$

where E_A is the activation energy, n is the diode ideality factor, J_{00} is the reverse saturation current pre-factor, and J_L is the photocurrent. In general, the activation energy E_A and J_{00} depend mainly on the dominating recombination mechanism in the solar cells. The activation energy (E_A) of the dominating recombination mechanism can be obtained from the $T = 0$ K intercept (see Fig. 9). From the V_{oc} *versus* temperature measurement we observed a significant difference between E_g and E_A values, showing that the loss mechanisms have not been fully remediated, and the dominating recombination mechanism is the interface recombination. The difference between E_g and E_A values was the highest in pure CZCTS and in ACZCTS with 15% Ag.

In kesterites the V_{oc} and also the V_{oc} deficit dependencies are more complex than in other materials. As was shown in ref. 43 the V_{oc} in kesterites is reduced by the existence of potential and band gap fluctuations, large ideality factors and low open-circuit collection efficiency. Therefore we can also expect that the activation energy obtained from V_{oc}–T dependencies is not completely correct. However, the measured activation energies E_A are about 300 meV smaller than the bandgap and therefore we believe that the interface recombination is prevailing in all samples.

For the detailed analysis of the solar cell characteristics, all the light J–V curves were fitted using a simple double diode model:

$$J = \sum_{i=1}^{2}\left(J_{0i}\left\{\exp\left[\frac{q(V+JR_S)}{n_i kT}\right]-1\right\}\right)+\frac{V+JR_S}{R_{\text{shunt}}}-J_L \quad (2)$$

where R_S is the series resistance, R_{shunt} is the shunt resistance, J_{01} and J_{02} are the saturation current densities for the first and second diode, and n_1 and n_2 are the ideality factors. The fitting was done using an algorithm proposed in ref. 44 and both ideality factors were not fixed during the fittings. Despite the good fit, unusual fit parameters for the second diode with quite high saturation current density J_{02} and ideality factor n_2 were obtained. This kind of current loss at higher voltages is a typical sign of recombination processes or the presence of crystals having very low performance, and thus the shape of the J–V curve of the second diode somehow represents these processes in the studied solar cells, see Fig. 10.

In order to understand the indicated recombination processes, the dependence of the ideality factor n_1 on temperature was studied. Temperature dependence of ideality factors in chalcopyrite based heterojunction solar cells was discussed in many papers, see for example ref. 45 and 46. However, there are still open questions when dealing with disordered kesterite based solar cells. It is known that these materials often have very high concentration of charged defects leading to quite deep electrostatic potential fluctuations. At the same time, the presence of the so-called disordered kesterite structure usually causes band gap fluctuations in the absorber and the depth of these fluctuations is more than 100 meV, introducing additional carrier recombination paths.[47] Moreover, temperature sensitive interface recombination contributes to current loss in kesterite materials, as was shown in ref. 48. All these factors affect the shape of the light J–V curves and the temperature dependence of the ideality factors.

The temperature dependence of ideality factor n_1 for 3 different samples is presented in Fig. 11.

It can be seen that the behavior of ideality factor is quite well fitted using the following formula:[46]

$$n = \frac{E_{00}}{kT}\coth\left(\frac{E_{00}}{kT}\right) \quad (3)$$

where $E_{00} = (q\hbar/2)\{N_A/(m \times \varepsilon)\}^{1/2}$ is the characteristic tunneling energy, N_A is the acceptor concentration and ε is a dielectric constant.[49] This type of temperature dependence of the ideality

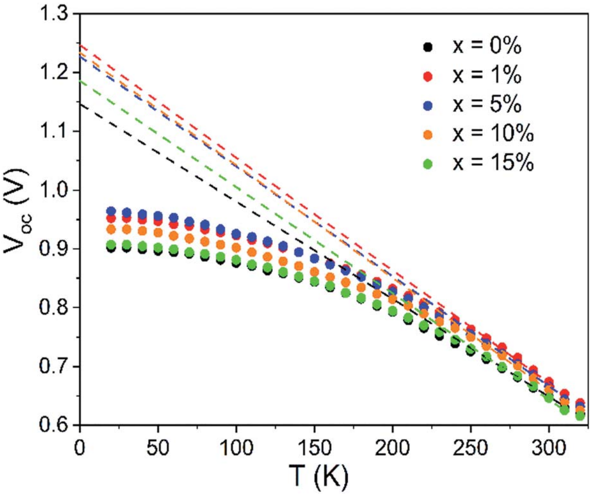

Fig. 9 V_{oc}–T measurements of the ACZCTS monograin powders with an input Ag content of 0 to 15%. Dashed lines present the extrapolation of the linear part of the V_{oc}–T at higher temperatures to the intercept with the y axis.

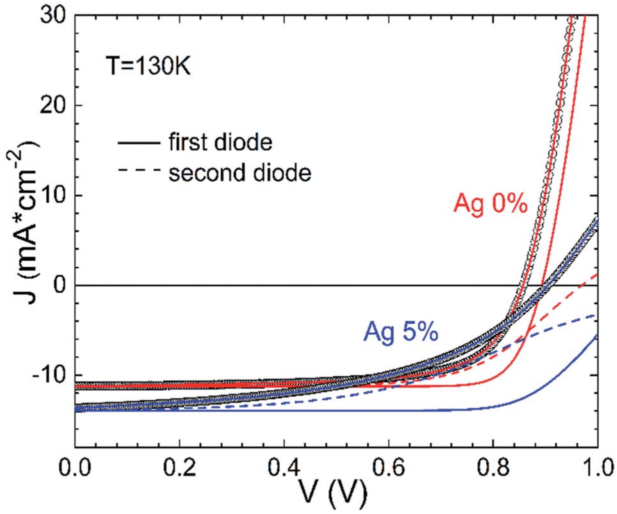

Fig. 10 Light J–V curves at $T = 130$ K for 2 samples with Ag contents of 0 and 5% together with fitting results using a double diode model, eqn (2). Solid and dashed lines represent the first and second diode, respectively.

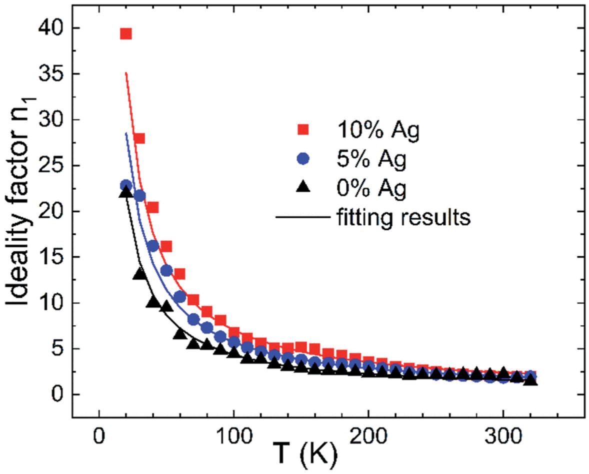

Fig. 11 The temperature dependence of ideality factor n_1 for 3 different samples together with the fitting result using eqn (3).

factor is typical of tunneling enhanced interface recombination, as was shown in ref. 46. In Table 1 the obtained tunneling energies E_{00} for the ACZCTS MGL solar cells with different Ag contents are presented. The tunneling energy first increased with increasing silver content, but at the highest silver concentration ($x = 15\%$) it decreased.

According to eqn (3), the increase of E_{00} can be explained by the increased acceptor concentration due to silver doping. It has been shown that the optimized Ag content in the CZTS absorber material leads to a decrease in the concentration of Cu_{Zn} anti-site defects.[4,6] Therefore, the detected increase in the acceptor concentration could result from the formation of Cu_{Cd} and Ag_{Zn} acceptor defects as is predicted by the DFT studies of Ag and Cd substitution of Cu and Zn in CZTS.[4] However, high concentration of silver probably leads to a compensation of acceptor defects as was also reported in previous reports.[4,7,8,34] Increasing the Ag incorporation into the absorber ($x = 15\%$) leads to a reduction in the carrier density and is considered to be the reason for poor junction formation. As a result, the solar cell performance decreases.

To summarize, it was found that by varying the Ag content in ACZCTS it is possible to modify the acceptor concentration in the absorber. Although it led to the increased V_{oc} values of the devices, the V_{oc} deficit remained unsolved. The input [Ag]/([Cu] + [Ag]) of 1% in monograin powder was found to be the optimum ratio to improve the optoelectronic properties of ACZCTS absorber materials, and the corresponding solar cells demonstrated a power conversion efficiency of 8.73%.

4. Conclusions

$(Cu_{1-x}Ag_x)_{1.85}(Zn_{0.8}Cd_{0.2})_{1.1}SnS_4$ monograin powders with different ratios of [Ag]/([Cu] + [Ag]) were successfully synthesized in molten KI and used as absorber materials in MGL solar cells. The Ag content in materials is variable, although the Ag content in synthesized powders was not equal to the input Ag concentration showing different distribution between liquid and solid phases. EDX analysis showed the Ag- and Cd-rich surface of the grains, while the Cu content on the surface was decreased compared to its constant value in the bulk of the monograins. The distribution coefficient of Ag between liquid KI and solid ACZCTS phases in the studied system can be characterized as the concentration ratio of Ag in the formed ACZCTS crystal surface crust and in the bulk and was found to be approximately equal to two ($[Ag]_{surface}/[Ag]_{bulk} = 2$ at 740 °C). The smallest tetragonal distortion with the lattice parameter ratio $c/2a = 0.9995$ was observed with the replacement of 1% Cu with Ag in ACZCTS. Raman spectra showed a shift in the Raman A peak position from 336 to 334 cm^{-1} as the Ag content increased in the monograin powder crystals. The band gap energy values showed a slight increase with the increase of Ag content; however the V_{oc} values of the ACZCTS device with the highest added Ag content ($x = 15\%$) decreased. Based on temperature dependent photoluminescence spectroscopy and J–V curve analysis, we conclude that by varying the Ag content in ACZCTS it is possible to modify the acceptor concentration in the absorber. Our findings confirm that the positive effect of Ag in ACZCTS MGL solar cells appears only at very low Ag concentrations ($x = 1\%$) and is detrimental to the solar cell performance at higher levels. The use of the optimal initial composition ([Ag]/([Cu] + [Ag]) ratio) for the growth of ACZCTS monograin powder crystals improved the efficiency of monograin layer solar cells from 6.62% ($x = 0\%$) to 8.73% ($x = 1\%$).

Conflicts of interest

There are no conflicts to declare.

Acknowledgements

This work was supported by the institutional research funding IUT (IUT19-28) of the Estonian Ministry of Education and Research and by the European Union through the European Regional Development Fund, Project TK141. The authors would also like to thank Dr J. Raudoja for his contribution to the synthesis-growth of monograin powders.

References

1 S. Giraldo, Z. Jehl, M. Placidi, V. Izquierdo-Roca, A. Pérez-Rodríguez and E. Saucedo, *Adv. Mater.*, 2019, **31**, 1806692.
2 W. Wang, M. T. Winkler, O. Gunawan, T. Gokmen, T. K. Todorov, Y. Zhu and D. B. Mitzi, *Adv. Energy Mater.*, 2014, **4**, 1301465.
3 E. Chagarov, K. Sardashti, A. C. Kummel, Y. S. Lee, R. Haight and T. S. Gershon, *J. Chem. Phys.*, 2016, **144**, 104704.
4 Z. K. Yuan, S. Chen, H. Xiang, X. G. Gong, A. Walsh, J. S. Park, I. Repins and S. H. Wei, *Adv. Funct. Mater.*, 2015, **25**, 6733–6743.
5 Y. Qi, Q. Tian, Y. Meng, D. Kou, Z. Zhou, W. Zhou and S. Wu, *ACS Appl. Mater. Interfaces*, 2017, **9**, 21243–21250.

6 Y. F. Qi, D. X. Kou, W. H. Zhou, Z. J. Zhou, Q. W. Tian, Y. N. Meng, X. S. Liu, Z. L. Du and S. X. Wu, *Energy Environ. Sci.*, 2017, **10**, 2401–2410.

7 S. Yang, S. Wang, H. Liao, X. Xu, Z. Tang, X. Li, T. Wang, X. Li and D. Liu, *J. Mater. Sci.: Mater. Electron.*, 2019, **30**, 11171–11180.

8 T. Gershon, Y. S. Lee, P. Antunez, R. Mankad, S. Singh, D. Bishop, O. Gunawan, M. Hopstaken and R. Haight, *Adv. Energy Mater.*, 2016, **6**, 1502468.

9 J. Fu, Q. Tian, Z. Zhou, D. Kou, Y. Meng, W. Zhou and S. Wu, *Chem. Mater.*, 2016, **28**, 5821–5828.

10 Z. Su, J. M. R. Tan, X. Li, X. Zeng, S. K. Batabyal and L. H. Wong, *Adv. Energy Mater.*, 2015, **5**, 1500682.

11 C. Yan, K. Sun, J. Huang, S. Johnston, F. Liu, B. P. Veettil, K. Sun, A. Pu, F. Zhou, J. A. Stride, M. A. Green and X. Hao, *ACS Energy Lett.*, 2017, **2**, 930–936.

12 S. Kim, K. M. Kim, H. Tampo, H. Shibata and S. Niki, *Appl. Phys. Express*, 2016, **9**, 102301.

13 A. D. Collord and H. W. Hillhouse, *Chem. Mater.*, 2016, **28**, 2067–2073.

14 S. Kim, K. M. Kim, H. Tampo, H. Shibata, K. Matsubara and S. Niki, *Sol. Energy Mater. Sol. Cells*, 2016, **144**, 488–492.

15 S. H. Hadke, S. Levcenko, S. Lie, C. J. Hages, J. A. Márquez, T. Unold and L. H. Wong, *Adv. Energy Mater.*, 2018, **8**, 1802540.

16 G. Sai Gautam, T. P. Senftle and E. A. Carter, *Chem. Mater.*, 2018, **30**, 4543–4555.

17 D. Braunger, D. Hariskos, G. Bilger, U. Rau and H. W. Schock, *Thin Solid Films*, 2000, **361–362**, 161–166.

18 I. Leinemann, K. Timmo, M. Grossberg, T. Kaljuvee, K. Tõnsuaadu, R. Traksmaa, M. Altosaar and D. Meissner, *J. Therm. Anal. Calorim.*, 2015, **119**, 1555–1564.

19 K. Timmo, M. Altosaar, M. Kauk, J. Raudoja and E. Mellikov, *Thin Solid Films*, 2007, **515**, 5884–5886.

20 K. Timmo, M. Altosaar, J. Raudoja, M. Grossberg, M. Danilson, O. Volobujeva and E. Mellikov, *2010 35th IEEE Photovoltaic Specialists Conference*, IEEE, 2010, pp. 001982–001985.

21 M. Kauk-Kuusik, K. Timmo, M. Danilson, M. Altosaar, M. Grossberg and K. Ernits, *Appl. Surf. Sci.*, 2015, **357**, 795–798.

22 C. Neubauer, E. Babatas and D. Meissner, *Appl. Surf. Sci.*, 2017, **423**, 465–468.

23 I. Klavina, T. Kaljuvee, K. Timmo, J. Raudoja, R. Traksmaa, M. Altosaar and D. Meissner, *Thin Solid Films*, 2011, **519**, 7399–7402.

24 L. Ratke and P. W. Voorhees, *Growth and Coarsening*, Springer Berlin Heidelberg, Berlin, Heidelberg, 2002.

25 M. Kauk, *Chemical Composition of $CuInSe_2$ Monograin Powders for Solar Cell Application*, Tallinn University of Technology Press, Tallinn, 2006.

26 I. Leinemann, G. C. Nkwusi, K. Timmo, O. Volobujeva, M. Danilson, J. Raudoja, T. Kaljuvee, R. Traksmaa, M. Altosaar and D. Meissner, *J. Therm. Anal. Calorim.*, 2018, **134**, 409–421.

27 K. Timmo, M. Kauk-Kuusik, M. Pilvet, V. Mikli, E. Kärber, T. Raadik, I. Leinemann, M. Altosaar and J. Raudoja, *Phys. Status Solidi A*, 2016, **13**, 8–12.

28 J. N. Bradley and P. D. Greene, *Trans. Faraday Soc.*, 1966, **62**, 2069.

29 M. Hassan, A. N. Al-hakimi and Rafiuddin, *Arabian J. Chem.*, 2011, **4**, 45–49.

30 K. Timmo, M. Kauk-Kuusik, M. Pilvet, M. Altosaar, M. Grossberg, M. Danilson, R. Kaupmees, V. Mikli, J. Raudoja and T. Varema, *Sol. Energy*, 2018, **176**, 648–655.

31 W. Gong, T. Tabata, K. Takei, M. Morihama, T. Maeda and T. Wada, *Phys. Status Solidi A*, 2015, **12**, 700–703.

32 T. H. Nguyen, T. Kawaguchi, J. Chantana, T. Minemoto, T. Harada, S. Nakanishi and S. Ikeda, *ACS Appl. Mater. Interfaces*, 2018, **10**, 5455–5463.

33 Y. Zhao, X. Han, B. Xu, W. Li, J. Li, J. Li, M. Wang, C. Dong, P. Ju and J. Li, *IEEE J. Photovoltaics*, 2017, **7**, 874–881.

34 W. Huang, S. Wei, C. Cai, W. Ho and C. Lai, *J. Mater. Chem. A*, 2018, **6**, 15170–15181.

35 D. Shin, B. Saparov and D. B. Mitzi, *Adv. Energy Mater.*, 2017, **7**, 1602366.

36 M. R. Balboul, H. W. Schock, S. A. Fayak, A. A. El-Aal, J. H. Werner and A. A. Ramadan, *Appl. Phys. A: Mater. Sci. Process.*, 2008, **92**, 557–563.

37 J. Just, D. Lützenkirchen-Hecht, R. Frahm, S. Schorr and T. Unold, *Appl. Phys. Lett.*, 2011, **99**, 262105.

38 K. Wang, O. Gunawan, T. Todorov, B. Shin, S. J. Chey, N. A. Bojarczuk, D. Mitzi and S. Guha, *Appl. Phys. Lett.*, 2010, **97**, 143508.

39 R. B. V. Chalapathy, G. S. Jung and B. T. Ahn, *Sol. Energy Mater. Sol. Cells*, 2011, **95**, 3216–3221.

40 M. Pilvet, M. Kauk-Kuusik, M. Altosaar, M. Grossberg, M. Danilson, K. Timmo, A. Mere and V. Mikli, *Thin Solid Films*, 2015, **582**, 180–183.

41 J. Krustok, R. Josepson, T. Raadik and M. Danilson, *Phys. Rev. B: Condens. Matter Mater. Phys.*, 2010, **405**, 3186–3189.

42 J. Krustok, R. Josepson, M. Danilson and D. Meissner, *Sol. Energy*, 2010, **84**, 379–383.

43 C. J. Hages, N. J. Carter, R. Agrawal and T. Unold, *J. Appl. Phys.*, 2014, **115**, 234504.

44 S. Suckow, T. M. Pletzer and H. Kurz, *Prog. Photovoltaics Res. Appl.*, 2014, **22**, 494–501.

45 U. Rau, A. Jasenek, H. Schock, F. Engelhardt and T. Meyer, *Thin Solid Films*, 2000, **361–362**, 298–302.

46 V. Nadenau, U. Rau, A. Jasenek and H. W. Schock, *J. Appl. Phys.*, 2000, **87**, 584–593.

47 M. Grossberg, J. Krustok, J. Raudoja and T. Raadik, *Appl. Phys. Lett.*, 2012, **101**, 102102.

48 M. Danilson, E. Kask, N. Pokharel, M. Grossberg, M. Kauk-Kuusik, T. Varema and J. Krustok, *Thin Solid Films*, 2015, **582**, 162–165.

49 F. A. Padovani and R. Stratton, *Solid-State Electron.*, 1966, **9**, 695–707.